

An adaptive-size multi-domain pseudospectral approach for solving the time-dependent Schrödinger equation

R. Esteban Goetz,¹ Andrea Simoni,² and Christiane P. Koch^{1,*}

¹*Theoretische Physik, Universität Kassel, Heinrich Plett-Straße 40, 34132 Kassel, Germany*

²*Institut de Physique de Rennes, UMR 6251, CNRS and Université de Rennes 1, 35042 Rennes Cedex, France*

(Dated: March 10, 2022)

We show that a pseudospectral representation of the wavefunction using multiple spatial domains of variable size yields a highly accurate, yet efficient method to solve the time-dependent Schrödinger equation. The overall spatial domain is split into non-overlapping intervals whose size is chosen according to the local de Broglie wavelength. A multi-domain weak formulation of the Schrödinger equation is obtained by representing the wavefunction by Lagrange polynomials with compact support in each domain, discretized at the Legendre-Gauss-Lobatto points. The resulting Hamiltonian is sparse, allowing for efficient diagonalization and storage. Accurate time evolution is carried out by the Chebyshev propagator, involving only sparse matrix-vector multiplications. Our approach combines the efficiency of mapped grid methods with the accuracy of spectral representations based on Gaussian quadrature rules and the stability and convergence properties of polynomial propagators. We apply this method to high-harmonic generation and examine the role of the initial state for the harmonic yield near the cutoff.

I. INTRODUCTION

Over the past decades, the field of quantum molecular dynamics has been driven by the development of efficient numerical methods for solving the time-dependent Schrödinger equation [1]. Current applications include studies of quantum optimal control [2] or electron dynamics. The two basic tasks that need to be addressed in quantum molecular dynamics are the representation of the state vector (and operators acting on it) and its time evolution. Ideally, the accuracy with which both tasks are accomplished should be balanced [3]. High accuracy is required by many state-of-the-art applications, for example in quantum optimal control [2]. At the same time, the exponential scaling of quantum dynamics calculations is a challenge for even the most advanced computer architectures. Efficiency of the methods is therefore also an issue, in addition to accuracy.

Highly accurate methods are obtained by employing pseudospectral approaches based on the expansion in orthogonal polynomials [4]. The representation problem can be solved using discrete variable representations or their unitary equivalent, finite basis representations [5]. The operators acting on the wavefunction are then given as sparse (often diagonal) matrices in one of the representations. The numerical effort is either due to the unitary transformation connecting the two representations or due to sparse matrix-vector multiplications. For a sufficiently large number of basis functions, the error becomes smaller than machine precision [6].

Polynomial approximations yield also the most accurate and stable propagation schemes [7]. Again, convergence is exponential with increasing polynomial order. For coherent time evolution, the best polynomial

approximation of the evolution operator is obtained by the Chebyshev propagator [8], while Newton polynomials yield an accurate and efficient propagator for open quantum systems [7]. Modifications of polynomial propagators allow to also accurately account for time ordering in case of a time-dependent Hamiltonian [9–11].

The high accuracy of these methods may, however, be compromised in time-dependent studies of dissociation or ionization where a sufficiently large grid, respectively a sufficiently large number of basis functions, becomes computationally prohibitive, both in terms of storage requirements and CPU time. Remedies to this problem include the use of variable grid steps [12–15] or variable-grid boundary conditions [16], wavefunction splitting methods [17–19], mask functions [20–22] or complex absorbing potentials (CAPs) [23, 24]. While the latter approach allows for calculating physical observables that require long propagation times [25–27], a CAP can only absorb wavepacket components within a certain frequency range [24]. It is thus rather difficult to completely avoid reflection which compromises accuracy. The problem of reflection also occurs for the mask function approach [16]. A CAP, moreover, renders the Hamiltonian non-Hermitian, which results in substantial technical difficulties for quantum optimal control [28–30] and may even preclude the evaluation of observables of interest [25, 26, 31]. Non-Hermitian Hamiltonians are avoided when using variable grid steps or wavefunction splitting but also in these cases high accuracy and reasonable numerical costs are not always guaranteed. For example, the mapped Fourier grid method [13–15, 32] was developed for long-range potentials that vanish asymptotically as $1/R^N$. It allows for an accurate description of most bound states and low-energy scattering states. However, the calculation of the bound spectrum does not scale favorably with the number of grid points, rendering its application in coupled channel calculations difficult [33, 34]. Moreover, it cannot be used in photoionization studies

* christiane.koch@uni-kassel.de

where high-energy scattering states may come into play. Wavefunction splitting is applicable in this case [19, 30]; it neglects, however, the Coulomb interaction between photoion and photoelectron. Thus, it cannot be used to study processes where recombination of the photoelectron is crucial, such as high harmonic generation. Here, we use a weak formulation [4, 35] of the Schrödinger equation to derive a sparse, yet accurate representation of the Hamiltonian and combine it with the Chebyshev propagation method [8]. The basic idea is to decompose the spatial domain into multiple sub-intervals of increasing size, chosen according to the local de Broglie wavelength, similar to the choice of the variable grid step in the mapped Fourier grid method [13–15, 32]. Within each interval, the wavefunction is expanded into Lagrange polynomials. The resulting representation of the Hamiltonian is sparse which is exploited in storage, diagonalization and matrix-vector operations [36]. Our approach thus combines the high accuracy of pseudospectral methods with the ability to use a very large spatial domain. It is particularly advantageous for quantum dynamics involving long-range potentials and long propagation times. As an example, we consider a laser-driven electron in a soft Coulomb potential, a popular model for high-harmonic generation.

The paper is organized as follows. Section II presents the method, starting with a brief review of the Chebyshev propagator. The pseudospectral multi-domain representation of the Hamiltonian is derived from the weak formulation of the Schrödinger equation in Section II A. Within each domain, a Gauss-Lobatto-Legendre collocation is employed, as described in Section II B, and a global representation of the Hamiltonian is derived in Section II C by assembling all domains. In section III, we present and compare numerical results between the MFGH and the MFGH-SEM. Section IV is devoted to time dependent results. Finally, summarizing remarks are outlined in Section V.

II. METHOD

The time-dependent Schrödinger equation reads

$$i\hbar \frac{\partial}{\partial t} \Psi(r, t) = \hat{H} \Psi(r, t), \quad (1)$$

where the Hamiltonian,

$$\hat{H} = -\frac{\hbar^2}{2m} \nabla^2 + V(r, t), \quad (2)$$

may contain a time-dependent term. The formal solution is given by

$$\begin{aligned} \Psi(r, t) &= \hat{T} \exp\left(-\frac{i}{\hbar} \int_0^t \hat{H}(\tau) d\tau\right) \Psi(r, 0) \\ &= \hat{U}(t) \Psi(r, 0). \end{aligned} \quad (3)$$

Polynomial propagators expand the evolution operator, $\hat{U}(t)$, as a function of the Hamiltonian, in a truncated

polynomial series [8, 10, 37]. To this end, the domain of the eigenvalues, i.e., the spectral radius of the Hamiltonian ΔE , must be known. Consider the example of a time-independent Hamiltonian in which case the Chebyshev propagator is simply obtained as

$$\hat{U}(t) = e^{-i\hat{H}t/\hbar} \approx \sum_{n=0}^N a_n T_n\left(-i\hat{H}t/\hbar\right). \quad (4)$$

Since the complex Chebyshev polynomials are defined in the interval $[-i, i]$, the Hamiltonian must be renormalized,

$$\hat{H}_{norm} = \frac{2\left(\hat{H} - \mathbb{1}(\Delta E/2 + V_{min})\right)}{\Delta E}.$$

The expansion coefficients a_n are known analytically [8] and the Chebyshev polynomials can be computed using their recursion formula. The solution is thus obtained by subsequent applications of the (renormalized) Hamiltonian to a wavefunction [3, 7, 8]. For a prespecified error, the number of Chebyshev polynomials, i.e., the number of times the Hamiltonian is applied to a wavefunction, is determined by the product of spectral radius ΔE and time step [3, 7, 8]. If the Hamiltonian has a matrix representation, the propagation involves a series of matrix-vector multiplications, $\hat{H}_{norm} \Psi_n(r, 0)$.

Here, we derive a sparse representation of the Hamiltonian (2). It is based on domain decomposition [4, 38, 39], the variational or weak solution [35] of the Schrödinger equation, Lagrange interpolation [4, 40], and polynomial series expansions of operators [3, 7, 8]. The concept of the local de Broglie wavelength, central to the mapped Fourier grid Hamiltonian [13–15, 32], is used to determine the size of the domains.

A. Multi-domain weak formulation

In order to derive a matrix representation of the Hamiltonian (2), we consider the time-independent radial Schrödinger equation,

$$-\frac{\hbar^2}{2\mu} \nabla^2 u(r) + V(r)u(r) = \lambda u(r) \quad (5)$$

with $r \in \Omega = [r_{min}, r_{max}]$ and λ an eigenvalue. We employ domain decomposition for Ω . The main idea behind this method is to split the domain of (spatial) integration Ω into M non-overlapping intervals, or 'elements', Ω_k of arbitrary size. The total domain, Ω , is constructed from the union of the M non-overlapping elements,

$$\Omega = \bigcup_{k=1}^M \Omega_k \text{ with } \Omega_k \cap \Omega_{k'} = \begin{cases} \{r_N^k\} & \text{if } k' = k + 1, \\ \emptyset & \text{otherwise,} \end{cases} \quad (6)$$

where $r_N^k = r_0^{k+1}$ and each interval $\Omega_k = [r_0^k, r_N^k]$ will be discretized using $N + 1$ points, and the constraint

$r_N^k = r_0^{k+1}$ ensures connection of all Ω_k . Within each interval $\Omega_k \in \Omega$, Eq. (5) becomes

$$-\frac{\hbar^2}{2\mu}\nabla^2 u^k(r) + V(r)u^k(r) = \lambda u^k(r). \quad (7)$$

with $r \in \Omega_k$. In order to derive the weak solution of the Schrödinger equation for a given Ω_k , we multi-

ply both sides of Eq. (7) by an arbitrary test function, $v^k(r) \in H^1(\Omega_k)$, where $H^1(\Omega^k)$ refers to the Sobolev space defined as

$$H^1(\Omega^k) = \left\{ \phi \in L^2(\Omega^k), \nabla\phi \in L^2(\Omega) \right\}. \quad (8)$$

Integrating over the domain Ω_k and applying Green's theorem, we find

$$-\frac{\hbar^2}{2\mu} \int_{\Omega_k} \nabla v^k(r) \nabla u^k(r) dr + \int_{\Omega_k} v^k(r) V(r) u^k(r) dr + \frac{\hbar^2}{2\mu} \oint_{\partial\Omega_k} v^k(r) \nabla_n u^k(r) d\Gamma = \lambda \int_{\Omega_k} v^k(r) u^k(r) dr, \quad (9)$$

where ∇ denotes the usual gradient and ∇_n stands for the normal derivative. The solution $u^k(r)$ satisfying Eq. (9) is called the *weak solution* on Ω_k , as opposed to the strong solution, i.e., $u^k(r)$ satisfying Eq. (7). Note that $u^k(x) \in H^1(\Omega_k)$. The weak solution of the Schrödinger equation in the weak formulation is obtained by deter-

mining $u^k(x) \in H^1(\Omega_k)$ and λ such that

$$\begin{cases} a^k(u, v) = \lambda(u, v)_{\Omega_k} \\ u(r) = \tilde{u}(r) \quad \text{in} \quad \partial\Omega_k, \end{cases} \quad (10a)$$

where $\tilde{u}(r)$ stands for the boundary condition of u^k at the domain boundary, $\partial\Omega_k$, and the bilinear forms, $a^k(\cdot, \cdot)$ and $(\cdot, \cdot)_{\Omega_k}$ are defined as follows,

$$a^k(u, v) = \frac{\hbar^2}{2\mu} \int_{\Omega_k} \nabla v^k(r) \nabla u^k(r) dr + \int_{\Omega_k} v^k(r) V^k(r) u^k(r) dr + \frac{\hbar^2}{2\mu} \oint_{\partial\Omega_k} v^k(r) \nabla_n u^k(r) d\Gamma, \quad (10b)$$

$$(u, v)_{\Omega_k} = \int_{\Omega_k} u^k(r) v^k(r) dr. \quad (10c)$$

In order to derive an explicit representation of the Hamiltonian from the weak formulation of the Schrödinger equation, we rewrite the bilinear forms as a linear operator equation in dual space. To this end, we employ a Galerkin-type method based on piecewise cardinal functions with bounded support in Ω_k , $\delta^k(r - r_j)$ where $r_j \in \Omega_k$.

B. Gauss-Lobatto-Legendre collocation

Consider the vector space spanned by $N + 1$ cardinal functions defined within Ω_k and denote the set of basis functions by $\{v_j^k\}_{j=0, \dots, N}$. We can expand $u^k(r)$ in this basis,

$$u^k(r) = \sum_{j=0}^N u^k(r_j) v_j^k(r) = \sum_{j=0}^N u^k(r_j) \delta^k(r - r_j). \quad (11)$$

Inserting Eq. (11) into Eq. (9), multiplying both sides of Eq. (9) by one of the cardinal functions and integrating

over Ω_k , we find a set of $N + 1$ algebraic equations,

$$\sum_{j=0}^N u_j^k a^k(v_i, v_j) = \lambda \sum_{j=0}^N u_j^k (v_i, v_j)_{\Omega_k}, \quad (12)$$

where $i = 0, \dots, N$, $u_j^k = u^k(r_j)$ and $r_j \in \Omega_k$ by construction.

In the particular case of a discrete variable representation [5, 41], the expansion coefficients $u^k(r_j)$ in Eq. (11) correspond to the wavefunction amplitudes at every collocation point and the error is only due to the Gaussian quadrature approximation. In other words, in each domain Ω_k , $u^k(r)$ is approximated at the collocation points by the interpolant in Eq. (11). Correspondingly, we can evaluate the integrals in Eq. (10b) by means of a Gaussian quadrature rule within each interval Ω_k ,

$$\int_{\Omega_k} f(r) dr = \sum_{j=0}^N f^k(r_j) w_j^k. \quad (13)$$

This leads to

$$a^k(v_i, v_j) \approx \frac{\hbar^2}{2\mu} \sum_{q=0}^N \nabla v_i^k(r_q) \nabla v_j^k(r_q) w_q^k + \sum_{j=0}^N v_i^k(r_q) V(r_q) v_j^k(r_q) w_q^k + \frac{\hbar^2}{2\mu} (\nabla u^k(r_0^k) \delta_{0,i} - \nabla u^k(r_N^k) \delta_{N,i}), \quad (14a)$$

Using Gauss-Lobatto sampling points, i.e., sampling points that include the boundary of the domain Ω_k , by definition $v_i^k(r_0^k) = \delta_{0,i}$ and $v_j^k(r_N^k) = \delta_{N,i}$ for $k = 2, \dots, M-1$, i.e., for all domains except those containing r_{min} and r_{max} . Analogously, for Eq. (10c) we use the discrete inner product in Ω_k which is given by

$$(v_i, v_j)_{\Omega_k} \approx \sum_{q=0}^N u_i^k(r_q) v_j^k(r_q) w_q^k = w_i^k \delta_{i,j}. \quad (14b)$$

We will employ Gaussian quadrature based on Legendre polynomials. Since Legendre polynomials are defined on the interval $\Lambda = [-1, 1]$, we need an affine transformation,

$$\begin{aligned} \Phi^k : \Lambda &\longrightarrow \Omega_k \\ \xi_i &\longmapsto \xi_i (r_N^k - r_0^k) / 2 + (r_N^k + r_0^k) / 2. \end{aligned} \quad (15a)$$

with Jacobian

$$\mathcal{J}_k = (r_N^k - r_0^k) / 2 \quad (15b)$$

and ξ_i the standard Gauss-Lobatto-Legendre sampling points, cf. Eq. (A4). Integration in Ω_k can then be directly connected to integration in Λ ,

$$\int_{\Omega_k} f(r) dr = \int_{-1}^{+1} f \circ \Phi^k(\xi) \mathcal{J}_k d\xi = \mathcal{J}_k \sum_{j=0}^N f(r_j) w_j^\Lambda.$$

Comparing this to Eq. (13), we find

$$w_j^k = \mathcal{J}_k w_j^\Lambda \quad (16)$$

with w_j^Λ that standard Legendre quadrature weights, cf. Eq. (A4).

Next, we evaluate the derivatives in Eq. (14a) in terms of derivatives of the cardinal functions,

$$\frac{\partial}{\partial r} f^k(r) = \sum_{j=0}^N f(r_j) \frac{\partial}{\partial r} \delta^k(r - r_j). \quad (17)$$

Using the properties of the Legendre polynomials and the cardinal functions, cf. Appendix A, the first order differentiation matrix for Legendre cardinal functions is found to read [4]

$$\frac{\partial}{\partial \xi} \delta^{(\Lambda)}(\xi_i - \xi_j) = \begin{cases} -N(N+1)/4 & \text{if } i = j = 0 \\ N(N+1)/4 & \text{if } i = j = N \\ 0 & \text{if } 1 \leq i = j \leq N-1 \\ \frac{L_N(\xi_i)}{L_N(\xi_j)(\xi_i - \xi_j)} & \text{if } j \neq i. \end{cases} \quad (18)$$

This, together with the affine transformation (15), allows to determine the derivatives in Eq. (14a) with an error that is solely due to the Gaussian quadrature approximation. Moreover, a useful expression to evaluate the first term in Eq. (14a), needed to construct the matrix representation of the kinetic operator in the Schrödinger equation, is given by

$$S_{\mu,\nu}^k = \int_{\Omega_k} \frac{\partial}{\partial r} \delta^k(r - r_\mu) \frac{\partial}{\partial r} \delta^k(r - r_\nu) dr^k$$

with $\mu, \nu = 0, \dots, N$. It is straightforward to show that

$$S_{\mu,\nu}^k = \mathcal{J}_k^{-1} S_{\mu,\nu}^\Lambda,$$

where

$$\begin{aligned} S_{\mu,\nu}^\Lambda &= \int_{\Lambda} \frac{\partial}{\partial \xi} \delta^\Lambda(\xi - \xi_\mu) \frac{\partial}{\partial \xi} \delta^\Lambda(\xi - \xi_\nu) d\xi \\ &\approx \sum_{j=0}^N \frac{\partial}{\partial \xi} \delta^\Lambda(\xi_j - \xi_\mu) \frac{\partial}{\partial \xi} \delta^\Lambda(\xi_j - \xi_\nu) w_j^\Lambda. \end{aligned} \quad (19)$$

The matrix S^Λ can be written as a product,

$$S^\Lambda = D(w) D^\dagger(w)$$

with

$$D_{i,j}(w) = \frac{\partial}{\partial \xi} \delta^\Lambda(\xi_i - \xi_j) \sqrt{w_i^\Lambda} \quad (20)$$

and the derivatives given in Eq. (18). Recall that at the Gauss-Lobatto-Legendre points, the cardinal functions, cf. Eq. (A7), obey

$$\delta^k(r_i - r_j) = \delta_{i,j},$$

where $\delta_{i,j}$ stands for the Kronecker delta. This, together with Eq. (19), yields the following algebraic expression

$$\sum_{j=0}^N u_j^k \left(\frac{\hbar^2}{2\mu} \mathcal{J}_k^{-1} S_{i,j}^\Lambda + V(r_j) \delta_{i,j} w_j^k \right) + \frac{\hbar^2}{2\mu} \nabla u(r_0^k) \delta_{0,i} - \frac{\hbar^2}{2\mu} \nabla u(r_N^k) \delta_{N,i} = \lambda \sum_{i=0}^N u^k(r_i) w_j^k \delta_{i,j}, \quad (21)$$

with $i = 0, \dots, N$ for the weak form of the Schrödinger equation, Eq. (12), within the domain Ω_k .

C. Global representation

Finally, we need to assemble all domains Ω_k , $k = 1, \dots, M$, in order to construct a global representation of the time-independent Schrödinger equation (5), and thus the Hamiltonian, from Eq. (21). Since $\Omega = \bigcup_{k=1}^M \Omega_k$, this can simply be done by adding the multi-domain bilinear

forms defined in Eqs. (10),

$$a(u, v) = \lambda(u, v) \Leftrightarrow \sum_{k=1}^M a^k(u, v) = \sum_{k=1}^M \lambda(u, v)_{\Omega_k}, \quad (22)$$

provided that the correct boundary conditions are ensured at the intersection of two contiguous elements,

$$r_N^k \stackrel{!}{=} r_0^{k+1}, \quad (23a)$$

$$u^k(r) \Big|_{r=r_N^k} \stackrel{!}{=} u^{k+1}(r) \Big|_{r=r_0^{k+1}}, \quad (23b)$$

$$\nabla u^k(r) \Big|_{r=r_N^k} \stackrel{!}{=} \nabla u^{k+1}(r) \Big|_{r=r_0^{k+1}}. \quad (23c)$$

Continuity and differentiability of the global solution need to be enforced since the global cardinal basis, defined as $v^k(r - r_N^k) \cup v^{k+1}(r - r_0^{k+1})$, is not differentiable at the $M - 1$ interelement points. Consider the sum of $a^k(u, v)$ for two contiguous elements,

$$\begin{aligned} a^k(u^k, v^k) + a^{k+1}(u^{k+1}, v^{k+1}) &= \frac{\hbar^2}{2\mu} \int_{\Omega_k} \nabla u^k(r) \nabla v^k(r) dr + b_{\Omega_k \cup \Omega_{k+1}} + \frac{\hbar^2}{2\mu} \int_{\Omega_{k+1}} \nabla u^{k+1}(r) \nabla v^{k+1}(r) dr \\ &+ \frac{\hbar^2}{2\mu} (v^k(r_0^k) \nabla u^k(r_0^k) - v^{k+1}(r_N^{k+1}) \nabla u^{k+1}(r_N^{k+1})) \\ &+ \frac{\hbar^2}{2\mu} (v^{k+1}(r_0^{k+1}) \nabla u^{k+1}(r_0^{k+1}) - v^k(r_N^k) \nabla u^k(r_N^k)), \end{aligned} \quad (24)$$

where we have defined

$$b_{\Omega_k \cup \Omega_{k+1}} = b^k(u^k, v^k) + b^{k+1}(u^{k+1}, v^{k+1}) \quad \text{with} \quad b^k(u^k, v^k) = \int_{\Omega_k} u^k(r) V(r) v^k(r) dr.$$

For the bilinear form $a(u, v)$, the condition of differentiability implies that the last term in Eq. (24) vanishes. Thus, when adding the bilinear forms for all intervals Ω_k , the interelement boundary conditions cancel out, as desired.

Analogously to Eq. (23) for the bilinear forms, we introduce the global interpolant $u(r)$ as

$$u(r) := \sum_{k=1}^M u^k(r) = \sum_{k=1}^M \sum_{j=0}^N u^k(r_j^k) v_j^k(r). \quad (25)$$

Then, just as the basis set expansion of $u^k(r)$, Eq. (11), has led to $N + 1$ algebraic equations within the interval Ω_k , Eq. (25) results in $M \times (N + 1)$ algebraic equations

for the total domain Ω ,

$$\sum_{k=1}^M \sum_{k'=1}^M \sum_{j=0}^N u_j^{k'} a^k(v_j^{k'}, v_i^q) = \lambda \sum_{k=1}^M \sum_{k'=1}^M \sum_{j=0}^N u_j^{k'} (v_j^{k'}, v_i^q)_{\Omega_k} \quad (26)$$

with $i = 0, \dots, N$, $q = 1, \dots, M$. Note that the subscripts i, j run over the collocation points whereas the superscripts k, k', q indicate the intervals. Since the cardinal functions $\delta^k(r - r_j)$ are non-zero only within their own interval Ω_k , we find

$$a^k(v_j^p, v_i^q) = a^k(v_j^k, v_i^k) \delta_{k,p} \delta_{p,q} \quad (27)$$

and

$$(v_j^p, v_i^q)_{\Omega_k} = w_i^k \delta_{k,p} \delta_{p,q} \delta_{i,j}. \quad (28)$$

Therefore, Eq. (26) takes the same form as Eq. (21) but with $(N+1) \times (M-1)$ vanishing terms. In other words, the global representation, by construction, is equivalent to writing the elemental equation (21) $M \times (N+1)$ times, i.e., as many times as there are configurations for the test function $v_j^k(r)$ with $j = 0, \dots, N$ and $k = 1, \dots, M$, while accounting for the boundary conditions (23). Specifically, when adding the two algebraic equations for $q = k, j = N$ and $q = k+1, j = 0$, for $k = 1, M-1$, in Eq. (26), the last (vanishing) term in Eq. (24) is retrieved at the $M-1$ connection points. We thus obtain a system of $M \times (N+1) - (M-1) = N \times M + 1$ algebraic equations, in accordance with the number of collocation points in the global representation, i.e., without any repetition of points.

Solving the linear system of equations (26) with the boundary conditions (23) is then equivalent to solving the generalized eigenvalue problem

$$A u = \lambda \mathcal{M}(w) u, \quad (29)$$

where $\mathcal{M}(w)$ is a $(N \times M + 1) \times (N \times M + 1)$ diagonal matrix, hereafter referred to as the *global mass matrix*. Its matrix elements are given in terms of the Gaussian quadrature weights w_j^k , cf. Eq. (16),

$$\mathcal{M}_{i,i}(w) = \gamma_j^k(w), \quad i = N(k-1) + j + 1, \quad (30a)$$

with $j = 0, \dots, N, k = 1, \dots, M$, and

$$\gamma_j^k(w) = \begin{cases} w_j^k & \text{if } k < M \text{ and } 0 < j < N, \\ w_N^k + w_0^{k+1} & \text{if } k \leq M \text{ and } j = 0, \\ w_N^{k-1} + w_0^k & \text{if } k < M \text{ and } j = N, \\ w_0^1 & \text{if } k = 1 \text{ and } j = 0, \\ w_N^M & \text{if } k = M \text{ and } j = N. \end{cases} \quad (30b)$$

Note that the weights defined at the interelement points, i.e., x_N^k and x_0^{k+1} , are defined as $w_N^k + w_0^{k+1}$. This can be easily shown by using the additivity theorem of integration for continuous functions. The matrix A corresponds to the global representation of the bilinear form $a(u, v)$. Because of the compact support of the basis functions $v_j^k(r)$, A is characterized by a sparse structure, with matrix elements

$$A_{i,j} = \begin{cases} a^k(v_{i'}^k, v_{j'}^k) & \text{if } i' \neq j' \neq 0 \text{ or } i' \neq j' \neq N, \\ a^1(v_0^1, v_0^1) & \text{if } k = 1, \\ a^M(v_N^M, v_N^M) & \text{if } k = M, \\ a^{k,k+1} & \text{if } k < M \text{ and } i' = j' = N, \\ a^{k-1,k} & \text{if } k \geq 2 \text{ and } i' = j' = 0, \\ 0 & \text{otherwise,} \end{cases} \quad (31a)$$

and global indices

$$i = N(k-1) + i' + 1 \text{ and } j = N(k-1) + j' + 1, \quad (31b)$$

such that $1 \leq i, j \leq NM + 1$ for $i', j' = 0, \dots, N$ and

$$a^{k,k+1} = a^k(v_N^k, v_N^k) + a^{k+1}(v_0^{k+1}, v_0^{k+1}). \quad (31c)$$

The *elemental* bilinear form $a^k(v_{i'}^k, v_{j'}^k)$, is given by

$$a^k(v_{i'}^k, v_{j'}^k) = \frac{\hbar^2}{2\mu} \mathcal{J}_k^{-1} S_{i',j'}^\Lambda + V(r_{i'}) \delta_{i',j'} w_{j'}^k + \frac{\hbar^2}{2\mu} \left(\nabla u(r_0^k) \delta_{0,j'} - \nabla u(r_N^k) \delta_{N,j'} \right), \quad (31d)$$

where $S_{i,j}^\Lambda$ is defined in Eq. (19) and \mathcal{J}_k^{-1} refers to the inverse of the Jacobian (15b).

Solution of Eq. (29) requires significantly less numerical effort, if \mathcal{M} can be transformed into identity. To this end, it suffices to renormalize the basis functions,

$$\tilde{v}_j^k(r) = \frac{\delta^k(r - r_j)}{\sqrt{\gamma_j^k}}, \quad (32)$$

Then, Eq. (11), i.e., the solution of Eq. (10a), takes the following form

$$u^k(r) = \sum_{j=0}^N \tilde{u}_j^k(r) \tilde{v}_j^k(x), \quad (33a)$$

with

$$\tilde{u}_j^k := u_j^k \times \sqrt{\gamma_j^k}. \quad (33b)$$

Using Eq. (33a), the linear system of equations (26) becomes

$$\sum_{k=1}^M \sum_{k'=1}^M \sum_{j=0}^N \tilde{u}_j^{k'} a^k(\tilde{v}_j^{k'}, \tilde{v}_i^q) = \lambda \sum_{k=1}^M \sum_{k'=1}^M \sum_{j=0}^N \tilde{u}_j^{k'} (\tilde{v}_j^{k'}, \tilde{v}_i^q)_{\Omega_k} \quad (34)$$

which is equivalent to solving

$$\tilde{A} \tilde{u} = \lambda \tilde{u} \quad (35)$$

with matrix elements

$$\tilde{A}_{i,j} = \frac{A_{i,j}}{\sqrt{\gamma_{i'}^k \gamma_{j'}^k}}, \quad (36)$$

where $A_{i,j}$ is given in Eq. (31a). The actual value of the eigenfunction at $r = r_j^k$ is obtained as $u_j^k = \tilde{u}_j^k / \sqrt{\gamma_j^k}$.

In order to explicitly state the global boundary conditions, it is convenient to rewrite Eq. (35) in the following form,

$$\tilde{H} \tilde{u} = \lambda \tilde{u} + \tilde{A}^{(0)} \tilde{u}, \quad (37a)$$

where $\tilde{A} = \tilde{H} - \tilde{A}^{(0)}$ and $\tilde{A}^{(0)} \tilde{u}$ denoting the boundary condition vector,

$$\begin{aligned} (\tilde{A}^{(0)} \tilde{u})_i &= \frac{\hbar^2}{2\mu} \left(-\nabla u(r_{i'}^k) \delta_{0,i'} \delta_{1,k} + \nabla u(r_N^k) \delta_{N,i'} \delta_{M,k} \right) \\ &= \frac{\hbar^2}{2\mu} \left(\nabla u(r_1) \delta_{i,1} - \nabla u(r_{NM+1}) \delta_{i,NM+1} \right) \end{aligned} \quad (37b)$$

with $i = i(i', k)$ found in Eq. (31b). In particular for bound states and eigenstates in a box, it is required that

$$u_0^1 = u_N^M = 0.$$

This can be enforced by the choice of basis functions, i.e., by ensuring $v_0^1 \stackrel{!}{=} 0$ and $v_N^M \stackrel{!}{=} 0$. A simple implementation is achieved by taking $j = 1, \dots, N$ for $k = 1$ and $j = 0, \dots, N - 1$ for $k = M$ instead of $j = 0, \dots, N$. The matrix representation of the Hamiltonian is then given by

$$\tilde{H}_{i-1,j-1} = \tilde{A}_{i,j}, \quad i, j = 2, \dots, NM.$$

$$H = \begin{pmatrix} \cdots & a_{N,N}^{k-2} + a_{0,0}^{k-1} & a_{0,1}^{k-1} & \cdots & a_{0,N}^{k-1} & 0 & 0 & 0 & 0 & \cdots & 0 & 0 & \cdots \\ \cdots & a_{0,1}^{k-1} & a_{1,1}^{k-1} & \cdots & a_{1,N}^{k-1} & 0 & 0 & 0 & 0 & \cdots & 0 & 0 & \cdots \\ \cdots & \vdots & \vdots & \ddots & \vdots & 0 & 0 & 0 & 0 & \cdots & 0 & 0 & \cdots \\ \cdots & a_{N,0}^{k-1} & a_{N,1}^{k-1} & \cdots & a_{N,N}^{k-1} + a_{0,0}^k & a_{0,1}^k & \cdots & a_{0,N}^k & 0 & \cdots & 0 & 0 & \cdots \\ \cdots & 0 & 0 & 0 & a_{1,0}^k & a_{1,1}^k & \cdots & a_{1,N}^k & 0 & \cdots & 0 & 0 & \cdots \\ \cdots & 0 & 0 & 0 & \vdots & \vdots & \ddots & \vdots & 0 & \cdots & 0 & 0 & \cdots \\ \cdots & 0 & 0 & 0 & a_{N,0}^k & a_{N,1}^k & \cdots & a_{N,N}^k + a_{0,0}^{k+1} & a_{0,1}^{k+1} & \cdots & a_{0,N}^{k+1} & 0 & \cdots \\ \cdots & 0 & 0 & 0 & 0 & 0 & \cdots & a_{1,0}^{k+1} & a_{1,1}^{k+1} & \cdots & a_{1,N}^{k+1} & 0 & \cdots \\ \cdots & 0 & 0 & 0 & 0 & \vdots & \vdots & \vdots & \vdots & \ddots & \vdots & 0 & \cdots \\ \cdots & 0 & 0 & 0 & 0 & 0 & 0 & a_{N,0}^{k+1} & a_{N,1}^{k+1} & \cdots & a_{N,N}^{k+1} + a_{0,0}^{k+2} & a_{0,1}^{k+2} & \cdots \\ 0 & 0 & 0 & 0 & 0 & 0 & 0 & 0 & 0 & 0 & a_{1,0}^{k+2} & a_{1,1}^{k+2} & \cdots \\ 0 & 0 & 0 & 0 & 0 & 0 & 0 & 0 & 0 & 0 & \vdots & \vdots & \ddots \end{pmatrix} \quad (38)$$

The sparsity and band-like structure can be exploited to reduce storage and CPU time in both diagonalization and time propagation, using standard libraries for sparse matrix-vector operations [36]. The number of matrix elements that need to be stored when exploiting the band-like structure is found to be

$$\mathcal{N}_{spar} = (N \times M + 1)(N + 1) - N(N + 1)/2 - 2(N + 1) \quad (39)$$

where $N + 1$ is the number of collocation points and M denotes the number of intervals. This compares to the $N_{pts}(N_{pts} + 1)/2$ different matrix elements of a full Hermitian matrix.

D. Choice of sub-intervals

The remaining question is how to choose the sub-intervals $\Omega_k = [r_0^k, r_N^k]$. As stated in Section II A, there is no a priori restriction on r_0^k and r_N^k for all $k = 1, \dots, M$. Here, we utilize the intuition underlying the Mapped Fourier Grid method [12, 13, 15, 32] and adapt the size of Ω_k to the local de Broglie wavelength. This implies that Ω_k gets larger in the asymptotic part of the potential.

It is achieved as follows. The overall domain Ω starts at r_{min} , i.e., $r_0^k = r_{min}$ for $k = 1$. The upper edge of the first interval, $r_N^{k=1}$, is obtained by solving the implicit

For Dirichlet boundary conditions, Eq. (37a) takes thus the form

$$\tilde{H} \tilde{u} = \lambda \tilde{u}.$$

Despite the dense structure of the matrix representation of the kinetic operator in each interval Ω_k , the local support of the basis functions $v_j^k(r)$ translates into a global kinetic energy matrix that is blockwise sparse except for the interelement points,

equation [15]

$$\beta = \frac{\sqrt{2\mu}}{\pi} \int_{r_0^k}^{r_N^k} \sqrt{E_{asy} - V(r)} dr, \quad (40)$$

where β and E_{asy} are two prespecified constants. For all further intervals Ω_k , r_0^{k+1} is set equal to r_N^k , and r_N^{k+1} is obtained by solving Eq. (40). This procedure is repeated until r_{max} is reached.

The two constants in Eq. (40) have a physical meaning, making their choice straightforward. The parameter β , $0 < \beta \leq 1$, estimates the local coverage of the phase space volume [15]: Smaller values of β result in a higher density of points, and $\beta = 1$ corresponds to the minimal classical estimation for the phase space discretization. The parameter E_{asy} specifies the smallest energy up to which the size of Ω_k is increased—if the grid includes r for which $V(r)$ is smaller than E_{asy} , the size of the intervals is kept constant.

Within each interval Ω_k , the points r_j^k , $j = 0, \dots, N$, are chosen according to the Legendre quadrature rule, as described in Section II B. Since each interval Ω_k is discretized by $N + 1$ collocation points, the density of points per element is constant. The resulting discretization is illustrated in Fig. 1 for the $B^1\Sigma_u^+$ electronically excited state of the Ca_2 molecule [42] which vanishes asymptotically as $1/R^3$. Such long-range states support extremely weakly bound vibrationally levels and therefore require

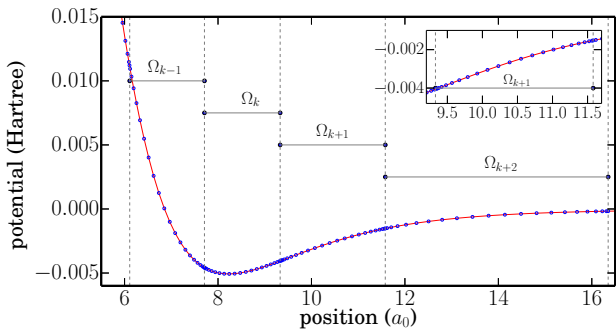


FIG. 1. Distribution of collocation points with $N = 21$. The inset shows a zoom onto the interval labeled by Ω_{k+1} . The high density of points close to the edges of the interval is typical for collocation based on Gauss-Lobatto-Legendre points.

large r_{max} to faithfully represent all bound levels [13]. Such levels are relevant for example in the photoassociation of ultracold atoms, and it was the need to calculate such levels that had prompted the development of the mapped Fourier grid method [13]. We will analyze the accuracy as well as the computational resources for the calculation of such levels with our multi-domain pseudospectral approach and compare it to the mapped Fourier grid method in Section III below before applying it in time-dependent calculations in Section IV.

III. CHOICE OF DOMAIN NUMBER AND COLLOCATION ORDER

The two parameters which are crucial for the analysis of accuracy and efficiency of the multi-domain pseudospectral approach are the number of intervals, M , and the number of collocation points within each interval $N+1$, or equivalently, the order of the interpolation polynomial, N . If M and N are chosen optimally, the calculation will be highly accurate while minimizing at the same time the requirements on storage and CPU time. The role of M and N in our approach is similar to the parameters h and p in finite element methods [4, 43–45], where the standard h -version, also referred to as h -refinement [4], consists in keeping the degree of the interpolating polynomials, usually of low degree, $p = 1, 2$, unchanged while modifying the size of each subdomain [4, 43–45]. Alternatively, the p -version, consists in keeping the size of each element unchanged while increasing the order of the interpolating polynomials [4, 43–45]. Finally, the h - p -version of the finite element method [43] modifies the size of each element only in regions where high resolution is needed [4].

As a first practical example, we consider the calculation of a weakly bound level of the $\text{Ca}_2 \text{B}^1\Sigma_u^+$ electronically excited state. The overall spatial domain is chosen with $r_{min} = 4.5 a_0$, $r_{max} = 50000 a_0$. For the

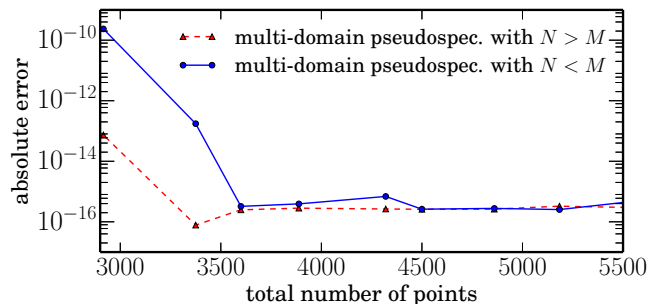


FIG. 2. Accuracy of the eigenvalue of a weakly bound level, calculated with the multi-domain pseudospectral method, referenced to the result obtained with the mapped Fourier grid Hamiltonian using a large number of points ($N_{pts} = 20000$). The reference eigenvalue is $E_{ref} = -2.2640245 \times 10^{-10}$ Hartree, compared to $E_0 \approx -2.607 \times 10^{-2}$ Hartree which is the eigenvalue with largest magnitude. When the total number of collocation points is sufficiently large, the accuracy of the multi-domain pseudospectral method is independent of the choice of the number of domains M and the collocation order N .

mapped Fourier grid Hamiltonian, we take the total number of grid points to be $N_{pts} = 20000$ which corresponds to $\beta = 0.029$. Choosing the eigenvalue labeled by $v_{ref} = 229$ with $E_{ref} = -2.2640249 \times 10^{-10}$ Hartree, we treat the result obtained with the mapped Fourier grid Hamiltonian and this very large number of points as a reference to benchmark the accuracy of the multi-domain spectral method for increasing the total number of collocation points, see Fig. 2. We find the calculation using the multi-domain spectral method to be converged to machine precision (with an arbitrary choice of N and M) if the total number of points, $N \times M + 1$, exceeds 3000. The overall precision in Fig. 2 is determined by the eigenvalue with the largest magnitude, which is the ground state of the Hamiltonian, with magnitude of the order of 10^{-2} Hartree. Machine precision relative to this value amounts to 10^{-17} Hartree. The accuracy of the pseudospectral method saturates somewhere about 10^{-16} Hartree. The missing digit is most likely due to different numerical routines for diagonalization in the multi-domain spectral method (with a sparse Hamiltonian matrix) and the mapped Fourier grid method (with a fully occupied Hamiltonian matrix).

An important question concerns the best choice of the parameters M and N . The same total number of points, $N \times M + 1$, can be realized by two different choices of M and N . Accuracy, storage requirement and spectral radius are, however, not the same between one configuration and the other. It is known from finite-element methods, that the p -refinement shows better convergence than the h -version [4]. In particular when just a small number of points is used, the accuracy may be improved by choosing $N > M$ [4]. Nevertheless, the imbalance between $N > M$ and $N < M$ is removed when the over-

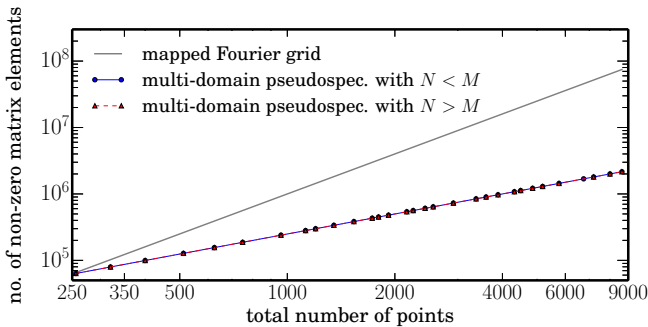


FIG. 3. Number of non-zero matrix elements of the Hamiltonian that need to be stored in memory. The mapped Fourier grid leads to a full kinetic energy matrix, whereas the Hamiltonian is sparse in the multi-domain pseudospectral representation. Note the log-log scale.

all number of points becomes sufficiently large, as shown in Fig. 2. Remarkably, the accuracy reaches a stationary value and remains independent of the choice of M and N . The corresponding flexibility in the choice of N and M is crucial for choosing optimal values for time propagation. On one hand, choosing larger N , i.e., a higher degree of the interpolation polynomial, and smaller M considerably reduces the total number of grid points, N_{pts} , for a given accuracy. Smaller N_{pts} decreases the spectral radius. On the other hand, our numerical tests show that the decrease of the spectral radius is actually even faster for the case of larger M and smaller N (with a correspondingly larger total number of points N_{pts}). We therefore focus on this second option and see in what follows that choosing a larger total number of points N_{pts} (with smaller N and larger M) does not compromise the efficiency of the Chebychev propagation nor increase the storage requirements for the Hamiltonian matrix.

The corresponding number of non-zero matrix elements of the Hamiltonian, i.e., the storage requirement, is shown in Fig. 3 as a function of the total number of points. Again, N and M have been chosen arbitrarily. Due to the sparsity of the Hamiltonian, the multi-domain pseudospectral representation requires significantly less storage than the mapped Fourier grid Hamiltonian. Given the fact, that the accuracy of both methods is the same for $N_{pts} > 3000$, the multi-domain pseudospectral representation allows for a dramatic reduction in the memory required to calculate the spectrum without compromising accuracy. This opens new perspectives for obtaining highly accurate weakly bound states as well as scattering states for long-range potentials, for example in coupled channels calculations, where the memory required for storing the mapped Fourier Hamiltonian quickly becomes a limiting issue [33, 34].

While different choices of N and M correspond to different storage requirements, this does not show up on the scale of Fig. 3. The sparsity of the Hamiltonian is therefore further analyzed in Fig. 4 by comparing the cases

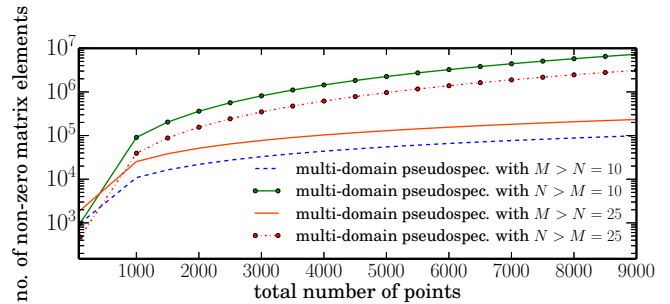


FIG. 4. Number of non-zero matrix elements of the Hamiltonian that need to be stored in memory for specific choices of N and M .

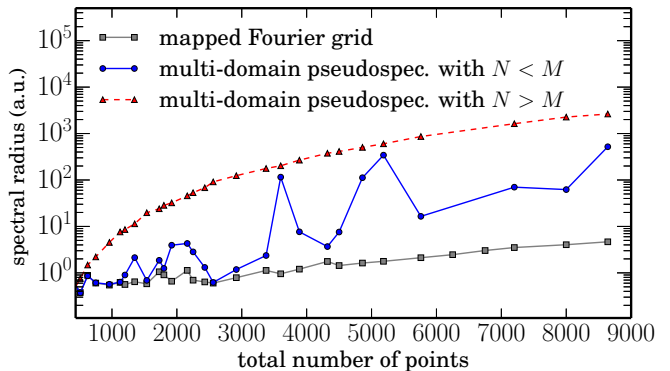


FIG. 5. Spectral radius as a function of the total number of points. The spectral radius determines the number of the times the Hamiltonian needs to be applied for time evolution with the Chebychev propagator.

$N > M$ and $N < M$ for a fixed number of points allowing, this time, N and M to be significantly different. As can be seen from Eq. (39), for a fixed number of points $N \times M + 1$, the case $N > M$ leads to a less sparse representation of the Hamiltonian matrix. However, both cases, $N > M$ and $N < M$, lead to a significant improvement in terms of storage, requiring only a few percent of the memory needed for the full matrix obtained with the mapped Fourier grid method.

Finally, we compare the spectral radius, ΔE , obtained with the mapped Fourier grid Hamiltonian and the adaptive multi-domain pseudospectral approach in Fig. 5. This is important because the spectral radius determines the number of terms in the Chebychev expansion of the time evolution operator, cf. Section II, i.e., the number of times the Hamiltonian is applied to a wavefunction. As a rule of thumb, the spectral radius of the mapped Fourier grid Hamiltonian is smaller than that obtained with the adaptive multi-domain pseudospectral approach for the same number of points. Moreover, we find that for the same N_{pts} , the spectral radius for $N > M$ is larger than that for $N < M$. This is somewhat unfortunate since

for a given total number of points better accuracy is obtained with $N > M$. However, since, for sufficiently large N_{pts} , the accuracy is independent of the choice of N and M , cf. Fig. 2, and time propagation will be most efficient for ΔE as small as possible, it is convenient to choose a relatively large total number of points with a low order N of the interpolation polynomial. This allows to reduce the numerical effort of the multi-domain pseudospectral method compared to the mapped Fourier grid Hamiltonian while keeping the level of accuracy, even though the total number of grid points required for the multi-domain pseudospectral approach is larger than that required for the mapped Fourier grid.

To summarize, it is optimal to (i) choose a low order of the interpolation polynomial or, equivalently, number of collocation points per element, e.g. $N = 3, 4, 5$, since it results in a small spectral radius, (ii) increase the total number of points such that the desired accuracy is obtained and (iii) define the number of intervals M according to $N_{pts} = N \times M + 1$.

Note that for a low order of the interpolation polynomials, e.g. $N = 3$, the sparse band-like structure of the kinetic energy matrix is quite similar to what is obtained using second and fourth order finite differences. We therefore compare the accuracy obtained with the multi-domain pseudospectral approach for low order of the interpolation polynomials to that of the second and fourth order finite differences. As shown in Fig. 6, the multi-domain pseudospectral representation yields a significantly better accuracy than finite differences. This reflects the *global* approximation of the derivatives within each interval and emphasizes the superiority of pseudospectral approaches over methods based on the Taylor expansion.

IV. APPLICATION TO HIGH HARMONIC GENERATION

We now apply our adaptive-size multi-domain pseudospectral propagation method to simulate high order harmonic generation. To this end, we consider an electron subject to a soft Coulomb potential [46],

$$V(x) = -\frac{1}{\sqrt{a+x^2}}. \quad (41)$$

The electron is subject to a linearly polarized electric field of the form

$$E(t) = E_0 G(t) \sin(\omega_0 t), \quad (42)$$

where $G(t)$ is a Gaussian envelope of full width at half maximum $\tau_{FWMH} = 206.5$ a.u., the maximal field amplitude is $E_0 = 0.06$ a.u., and the carrier frequency $\omega_0 = 0.1$ a.u. The interaction of the electron with the electric field is treated in the dipole approximation,

$$H_I(x, t) = -xE(t). \quad (43)$$

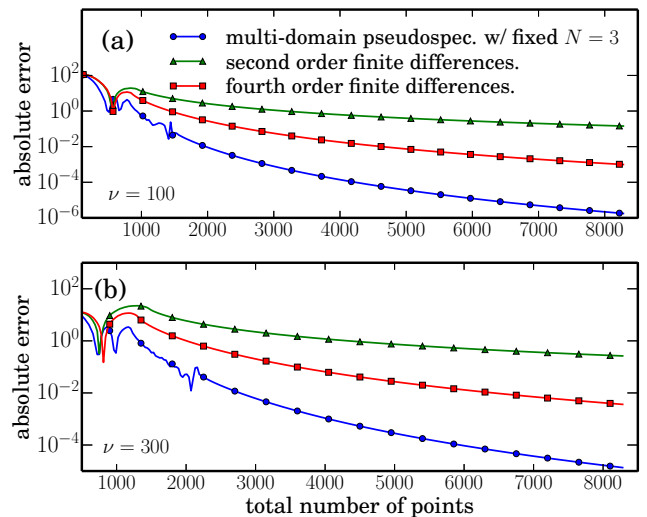


FIG. 6. Accuracy of the multi-domain pseudospectral approach for a low collocation order ($N = 3$) compared to second and fourth order finite differences for the levels $\nu = 100$ (a) and $\nu = 300$ (b) of the Morse potential with eigenvalues $E_{100} = -112.1253125$ a.u. and $E_{300} = -12.3753125$ a.u., respectively. Despite the similar structure of the Hamiltonian matrix, the pseudospectral approach is significantly more accurate.

The entire information about the harmonic generation process is encoded in the time-dependent dipole acceleration [47]. It is given by [48]

$$\ddot{d}(t) = \langle \psi(t) | \nabla_x V(x) | \psi(t) \rangle, \quad (44)$$

where the dependence on the external field is omitted since it does not contain higher harmonics. The harmonic spectrum $S(\omega)$ is obtained as [49]

$$S(\omega) = |\ddot{d}(\omega)|^2 / \omega^2, \quad (45)$$

where $\ddot{d}(\omega)$ is the Fourier transform of the dipole acceleration (44).

The electric field parameters given above lead to a ponderomotive energy [50] of $U_p = 0.16$ Hartree such that the Keldysh adiabaticity parameter [51] becomes $\gamma = 1.25$. Since with these parameters, $I_p > U_p > \omega_0$, where I_p is the ionization potential, the high harmonic generation process that we consider proceeds in the regime of above threshold ionization (ATI) [52]. Within the quasi-classical three-step model, the harmonic *cutoff* position is given by [53, 54]

$$\omega_c = (I_p + 3.17U_p) / \omega_0. \quad (46)$$

For an electron in the ground state, it becomes $\omega_c = 10.072$. The characteristic overestimation of the recollision probability of 1D models with respect to their counterpart 3D models is here minimized by the choice of a few-cycle pulse [48].

N	M	spectral radius [†]	CPU time [†]
10	270	973%	152%
6	450	411%	66%
5	540	310%	52%
4	675	227%	40%
3	900	165%	31%

[†] relative to mapped Fourier grid method

TABLE I. Numerical effort for wavepacket propagation with the adaptive-size multi-domain pseudospectral approach where N denotes collocation order and M the number of domains. The total number of collocation points is $N_{pts} = N \times M + 1 = 2701$. The reference calculation, using the mapped Fourier grid method and fast Fourier transforms, with 2047 grid points and a spectral radius of 1277.8 Hartree., took 959s of CPU time.

A. Numerical performance

First, we compare the numerical performance of the multi-domain pseudospectral method to that obtained with the mapped Fourier grid. In both cases, we utilize the Chebychev propagator, Eq. (4). For the multi-domain pseudospectral approach the Hamiltonian is applied via sparse matrix-vector multiplications, whereas the mapped Fourier grid method uses fast Fourier transforms together with vector-vector multiplications in real and momentum space.

We assume that initially the electron is in the ground state, $|\varphi_0\rangle$, of the field-free Hamiltonian. In particular, choosing $a = 2$ in Eq. (41) ensures that the ground state energy coincides with that of the true Coulomb potential, namely 0.5 Hartree. For the propagation based on the mapped Fourier grid, we use $R_{max} = 8000$ Bohr, which ensures that there are no spurious reflections at the edges of the grid during propagation. The remaining parameters are chosen to yield fully converged results. Specifically, we find the grid to be converged when using 2047 coordinate points, which leads to a correct representation of continuum states with energies well above $E_{max} = 0.25$ Hartree, the highest continuum state that gets populated during the dynamics.

The eigenvalues and eigenfunctions are obtained by diagonalization of the field-free Hamiltonian in the mapped Fourier grid representation. The set of eigenvalues from E_0 to E_{max} is used as a reference to define the accuracy of the mapped pseudospectral method, when testing several combinations of the number of domains, M , and collocation order N . We find that for a low collocation order, which minimizes the spectral radius, a larger number of total points is needed than with the mapped Fourier grid. For example, $N_{pts} = 2701$ for $M = 900$ and $N = 3$.

The dipole acceleration $\ddot{d}(t)$ and harmonic spectrum $S(\omega)$ obtained with both propagation approaches are depicted in Figs. 7(a) and (b), respectively. The few-cycle laser pulse indeed induces a fast dynamics of the electron, and the corresponding harmonic spectrum shows the characteristic cutoff. Clearly both methods yield the

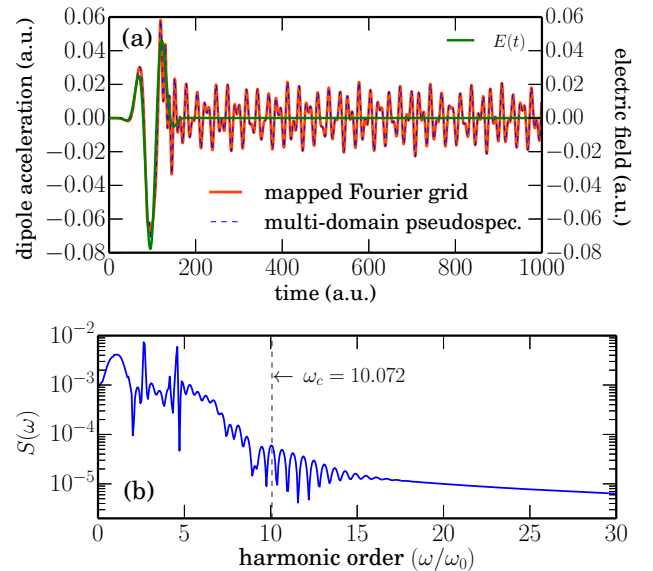


FIG. 7. (a) Time-dependent dipole acceleration $\ddot{d}(t)$ obtained with the mapped Fourier grid method and the multi-domain pseudospectral approach ($N = 3$, $M = 900$). For comparison, the electric field of the driving pulse is also shown. (b) Harmonic spectrum $S(\omega)$.

same dynamics, as expected. The numerical performance is, however, quite different. It is analyzed in Table I. Although the sparse structure of the Hamiltonian matrix in the multi-domain pseudospectral approach leads to a larger spectral radius, the CPU time required for propagation may be significantly smaller, depending on the collocation order N . Thus the multi-domain pseudospectral approach based on (sparse) matrix-vector multiplications is numerically more efficient than transforming the propagated wavepacket from coordinate to momentum representation by fast Fourier transforms, provided the parameters N and M are judiciously chosen.

The role of the spectral radius becomes particularly apparent for the choice $N = 10$ and $M = 270$ which leads to a propagation time 50 per cent longer than that needed with mapped Fourier grid approach, cf. Table I. In this case, the spectral radius is almost ten times larger than the one obtained with the mapped Fourier grid. Correspondingly, the number of terms in the Chebychev propagator, i.e., of applying the Hamiltonian, is ten-fold increased. However, choosing $N = 6$ and $M = 450$ reduces the spectral radius considerably, such that the CPU time for propagation is now only two thirds of that using the mapped Fourier grid method. Already for this choice of parameters, the adaptive-size multi-domain pseudospectral approach starts to be more efficient. The efficiency may be further improved by reducing N and increasing M , up to a third of the CPU time required with the mapped Fourier grid for $N = 3$ and $M = 900$.

Note that the accuracy in all cases is roughly the same,

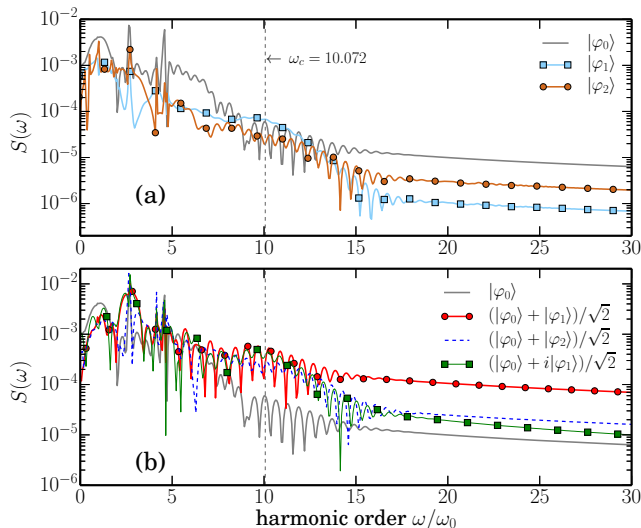


FIG. 8. Harmonic spectrum for different initial states: (a) Eigenstates of the field-free Hamiltonian and (b) superpositions of two field-free eigenstates.

since the overall number of collocation points is sufficiently large. A low collocation order N minimizes the spectral radius, and thus the number of terms in the Chebychev propagator. Larger N does not only lead to a larger spectral radius but also to a less sparse structure of the Hamiltonian, cf. Fig. 4, i.e., it results in a two-fold increase in the numerical cost. Since small N allows for highly accurate results, it is the preferable choice. In summary, the best performance of the multi-domain pseudospectral approach is achieved by choosing a relatively large total number of points, with small N and large M , such that the desired accuracy is obtained while minimizing the CPU time.

B. Enhancement of the high harmonic yield

We now employ the time-dependent multi-domain pseudospectral approach to analyzing the role of the initial state for the generation of the harmonic spectrum, while keeping the driving pulse fixed (using the same parameters as in Sec. IV A). This perspective is different from earlier studies [55–59] based on optimal control theory which modified the driving electric field to extend the harmonic cutoff and enhance the harmonic yield. Specifically, we seek to answer the question whether it is possible to enhance the yield of the harmonic spectrum at the harmonic cutoff by a suitable preparation of the initial state. We compare low-lying eigenstates of the field-free Hamiltonian as initial state and superpositions thereof. These different initial states could be prepared by a ‘pre-pulse’, preceding the pulse that drives the harmonic generation. In contrast, Refs. [56–59] only considered the ground state as initial state.

Figure 8(a) shows the harmonic spectra obtained for

the first three eigenstates $|\varphi_0\rangle$, $|\varphi_1\rangle$ and $|\varphi_2\rangle$ of the field-free Hamiltonian, with eigenenergies -0.500 Hartree, -0.233 Hartree and -0.134 Hartree, as initial state. The exponential decay instead of a plateau in Fig. 8(a) is characteristic of soft core potentials, the plateau being attributed to the singularity present in the Coulomb potential [60]. Since the ionization potential is the largest for the ground state, $|\varphi_0\rangle$ results in the largest harmonic cutoff, $\omega_c/\omega_0 = 10.1$ compared to 7.4 and 6.4 for the first and second excited state, respectively. Figure 8(a) also shows that the spectral yield of the high orders is largest for the ground state, particularly for higher photon energies.

Next, we consider, in Fig. 8(b), superpositions of field-free eigenstates as initial state and compare them to the best single eigenstate, $|\varphi_0\rangle$. It is worth mentioning that some precaution is necessary in the evaluation of the expectation value (44) since a superposition of eigenstates leads to a dipole acceleration even without any driving pulse. For instance, for a superposition of two states, this ‘‘field-free’’ dipole acceleration is given by

$$\ddot{d}_{ff}(t) = 2|a_i||a_j| \cos(\omega_{i,j}t - \vartheta) \langle \varphi_i | \nabla_x V(x) | \varphi_j \rangle \quad (47)$$

where $\hbar\omega_{i,j}$ is the energy difference between the superimposed states, ϑ their relative phase and $|a_k|$ the norm of the expansion coefficients. In order to analyze true high harmonics, we focus on the spectral yield for frequencies well above $\omega_{i,j}$, for example the yield close to the cutoff frequency.

We consider an equal superposition of two field-free eigenstates, allowing also for a complex phase. Figure 8(b) reveals, that depending on the expansion coefficients in the initial state, the harmonic yields is considerably enhanced, compared to the best single eigenstate, $|\varphi_0\rangle$. The superposition $(|\varphi_0\rangle + |\varphi_1\rangle)/\sqrt{2}$ does not only result in a higher harmonic yield at the cutoff, but also in a larger integrated spectrum, i.e., a larger integrated power density, for frequencies higher than ω_c . This is true not only for the comparison with the initial states shown in Fig. 8(b), but also for other superpositions.

The finding of Fig. 8(b) motivates a more thorough control study which is easily possible, given the numerical efficiency of the multi-domain pseudospectral approach. Specifically, we use optimization to determine the best combination of eigenstates, such that the power density of the harmonic yield starting from the cutoff ω_c is maximized. This choice ensures maximization of the total integrated spectrum for high harmonic orders beyond the cutoff. In detail, we employ the Sequential PArametrization (SPA) technique [61] to determine the expansion coefficients in the initial state, $c_j \in \mathbb{C}$, such that propagation of this state maximizes the integrated spectrum [56, 57],

$$J[c_j] = \int_{\omega_c}^{\omega_f} |\ddot{d}(\omega)|^2 d\omega. \quad (48)$$

The harmonic *cutoff* position ω_c is taken to be the one obtained for the ground state as initial state. The upper

limit is defined to be $\omega_f = 3\omega_c$. Note that the functional as defined in Eq. (48) does not only enhance the spectral yield in $[\omega_c, \omega_f]$, but it can also extend the harmonic cutoff as a function of ω_f .

We use $(|\varphi_0\rangle + |\varphi_1\rangle)/\sqrt{2}$ to start the optimization, since this superposition was found to considerably enhance the power spectrum. The SPA technique updates the expansion coefficients, which can take complex values, sequentially: Starting with two guess coefficients, $c_0 = c_1 = 1/\sqrt{2}$, additional coefficients are sequentially added, once a plateau is encountered in the optimization [61].

Upon optimization with only two states, we find the optimal initial superposition to be composed of $|\varphi_0\rangle$ and $|\varphi_1\rangle$ with coefficients $c_0 = 0.7215$ and $c_1 = 0.6924$. The resulting harmonic yield is very slightly better, by less than 1 per cent, than that obtained with equal weights, $c_0 = c_1 \approx 0.7071$, in the initial superposition. A similarly small improvement is obtained for a superposition involving $|\varphi_0\rangle$ and $|\varphi_2\rangle$. Including up to eight eigenstates in the initial superposition improves the value of the optimization functional (48) by 19 per cent compared to the superposition of $|\varphi_0\rangle$ and $|\varphi_1\rangle$ with equal weights. This improvement is, however, solely due to the smooth, exponentially decaying region (data not shown), where the harmonic yield is already small.

The role of the phase in the initial superposition is analyzed in Fig. 9. It displays the integrated spectrum within the interval $[\omega_c, 3\omega_c]$ as a function of the relative phase ϑ in the superposition,

$$|\varphi\rangle = \frac{1}{\sqrt{2}}(|\varphi_0\rangle + e^{i\vartheta}|\varphi_j\rangle) \quad (49)$$

for $j = 1, 2, 3$. For $j = 1$, maxima are found in Fig. 9(a) for $\vartheta \approx \pi/32$ and $\vartheta \approx 65\pi/64$ which result in the same maximal yield, differing from the yield for $\theta = 0, 2\pi$ by only ≈ 0.15 per cent. In contrast, the minimal yield observed in Fig. 9(a) differs by four orders of magnitude.

In order to elucidate the physical origin of the oscillations of the harmonic yield as a function of the relative phase in the initial superposition state, we compare the integrated spectrum (solid red lines in Fig. 9(a)) to the initial dipole acceleration (dashed grey line) which is a direct result of the superposition, cf. Eq. (47). Indeed, the oscillations of the spectral yield as a function of the superposition phase are strongly correlated to the absolute value of the initial dipole acceleration (grey dotted curve). Consider in particular the two initial states $|\varphi\rangle = (|\varphi_0\rangle \pm |\varphi_1\rangle)/\sqrt{2}$, i.e., $\vartheta = 0$ and $\vartheta = \pi$. These states are orthogonal and lead to equal initial dipole accelerations with opposite sign but slightly different spectral yields. This raises the question whether the sign of $\ddot{d}(t=0)$ determines the maximal value of the harmonic yield. In order to answer this question, we compare the integrated spectrum obtained with $-E(t)$ to that for $E(t)$ (blue dashed and red solid lines in Fig. 9(a)). The idea is that there is an effective “initial” time when the driving field starts to become non-zero. The superposition at

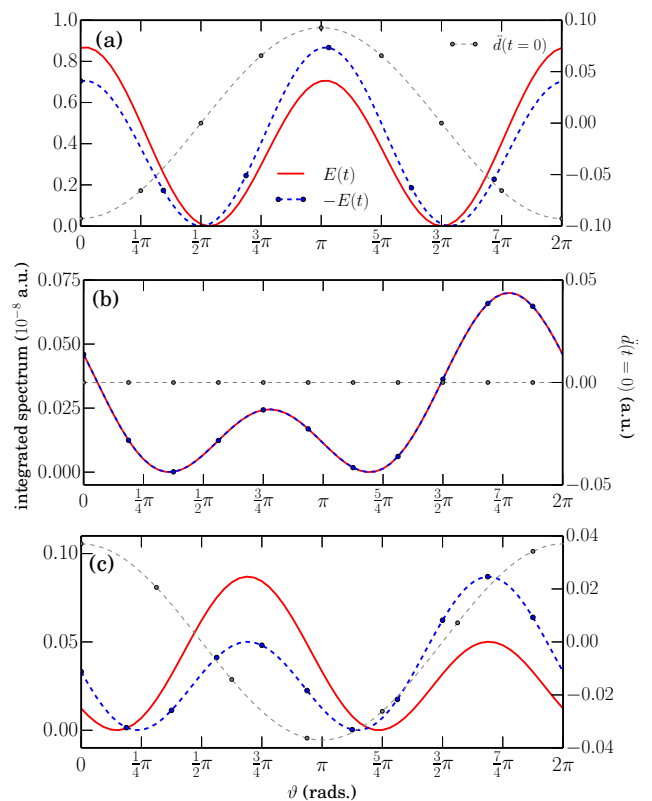


FIG. 9. Integrated spectrum (red solid and blue dashed curve, left-hand side label), cf. Eq. (48), and initial dipole acceleration (grey dotted curve, right-hand side label) as a function of the relative phase θ in Eq. (49) for initial superpositions of $|\varphi_0\rangle$ and $|\varphi_1\rangle$ (a), $|\varphi_0\rangle$ and $|\varphi_2\rangle$ (b) and $|\varphi_0\rangle$ and $|\varphi_3\rangle$ (c) with electric fields $E(t)$ (red solid curve) and $-E(t)$ (blue dashed curve).

$t = 0$ prepares an “initial” wave packet at that time or, classically spoken, the dipole acceleration at $t = 0$ determines the effective “initial” dipole acceleration at $t = t_p$. If the harmonic generation depends on both norm and sign of the dipole acceleration when the field starts to become non-vanishing, that is at $t = t_p$, a symmetric relationship should be found when changing the sign of $E(t)$ at $t = t_p$. This symmetry is indeed observed in Fig. 9(a), cf. the harmonic yield obtained with $\vartheta = \pi$ (giving a positive $\ddot{d}(0)$) and $-E(t)$, which matches exactly the yield for $\vartheta = 0$ (giving a negative $\ddot{d}(0)$) and $+E(t)$. Shifting the electric field according to $E(t - T_s)$ with $T_s = 2\pi/\omega_{0,1}$ so that $\ddot{d}_{ff}(t) = \ddot{d}_{ff}(t - T_s)$ does not change the spectral yield (data not shown). This is of course expected for an initial condition at $t_p - T_s$ that is identical to that at t_p .

To further investigate the dependence on the initial state, we consider a superposition of eigenstates of the same parity, i.e., $|\varphi_0\rangle$ and $|\varphi_2\rangle$, cf. Fig. 9(b). In fact, because $dV(x)/dx$ has odd parity, this superposition should lead to a vanishing initial dipole acceleration, cf.

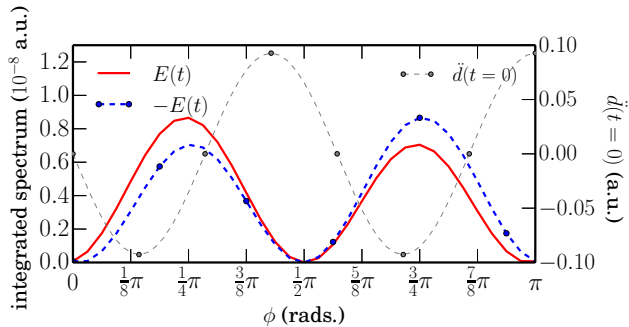


FIG. 10. Same as Fig. 9 but as a function of the relative amplitude of $|\varphi_0\rangle$ and $|\varphi_1\rangle$ in the initial superposition state, cf. Eq. (50).

Eq. (47). Therefore, the harmonic yield obtained with such an initial superposition should be not sensitive to a change of $E(t)$ to $-E(t)$, if the classical picture is still valid. This is indeed observed in Fig. 9(b). Similarly, the superpositions with vanishing initial dipole acceleration in Fig. 9(a) are also not sensitive to a change of $E(t)$ to $-E(t)$. While for a superposition of $|\varphi_0\rangle$ and $|\varphi_1\rangle$, peaks in the high harmonic yield are found for $\vartheta = 0$ and $\vartheta = \pi$, i.e., for a maximal initial dipole acceleration (in absolute value), such a correlation is not observed for the superposition of $|\varphi_0\rangle$ and $|\varphi_2\rangle$. In this case, the dependence of the high harmonic yield, for example the peak at $\vartheta = 7\pi/4$, cannot be explained based on a simple classical argument.

Figure 9(c) displays another example of an initial superposition of even and odd parity states ($|\varphi_0\rangle$ and $|\varphi_3\rangle$). While a similar dependence on the sign of the initial dipole acceleration is observed as in Fig. 9(a), in particular when changing the sign of the driving field, there is no one-to-one correlation between the high harmonic yield and the initial dipole acceleration. This shows that not only the initial dipole acceleration contributes to an enhancement of the high harmonic yield, but it also depends on the states involved in such a superposition.

Finally, we consider amplitude control of the initial superposition state. This can be expressed as a function of a rotation angle ϕ ,

$$|\varphi\rangle = \cos(\phi)|\varphi_0\rangle + \sin(\phi)|\varphi_1\rangle. \quad (50)$$

The high harmonic yield as a function of ϕ , i.e., the relative amplitude in a superposition of ground and first excited state is shown in Fig. 10. A correlation between the oscillations of the high harmonic yield and the initial dipole acceleration is observed, similar to that found in dependence on the relative phase. Also, an analogous symmetry when changing the sign of $E(t)$ is obtained. This shows that the control over the high harmonic yield can equally be achieved by controlling the relative phase or the relative amplitudes in the initial superposition state.

Enhancement of the high harmonic yield due to a purely quantum effect is in contrast with the fact that

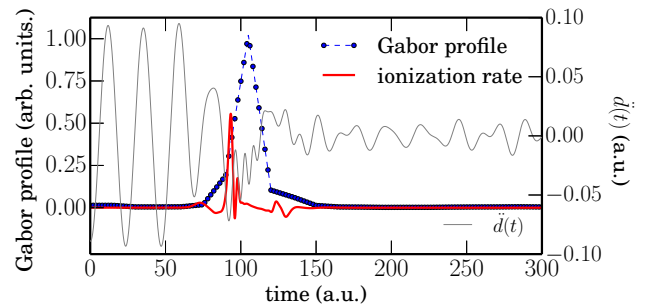


FIG. 11. Gabor profile of harmonics emitted with $\omega \in [\omega_c, 3\omega]$ for the initial superposition state $|\varphi\rangle = (|\varphi_0\rangle + |\varphi_1\rangle)/\sqrt{2}$. The generation of the high harmonic coincides with the temporal oscillations of the ionization rate, cf. full-red lines (scale not shown), in agreement with the three-step model. The grey line displays the dipole acceleration.

high harmonic generation is usually explained with the three-step model [53], i.e., using a semi-classical picture. We therefore verify whether the three-step model is still valid when starting from a superposition state. To this end, we plot in Fig. 11 the temporal Gabor profile of the harmonic yield corresponding to the frequency range above the cutoff and compare it to the ionization probability. The superposition of ground and first excited state, which results in the largest enhancement of the high harmonic yield, cf. Fig. 8, is used as initial state. As can be seen from Fig. 11, high harmonics are generated when the ionization probability is strongly time-dependent. The oscillations of the ionization probability (solid red line in Fig. 11) indicate that the propagated wavefunction, or part of it, populates the continuum and then returns to the ionic core. This process of ionization and recombination is repeated several times. It is exactly in coincidence with the oscillations in the ionization probability that high harmonics are emitted as revealed by the peak in the Gabor profile (blue dashed line). We thus find the process of high harmonic generation still to be well described by the three-step model, in which semi-classical electron motion leads to the emission of high harmonics [53]. This is in line with earlier findings that coherent control of high harmonic generation reduces to the problem of laser control over classical electron trajectories [54, 57].

The dependence of the high harmonic yield on the relative phase in the initial superposition points to constructive and destructive interference in the maximization of the dipole acceleration, a hallmark of coherent control. Controlling the harmonic yield by a suitable preparation of the initial state could be realized in an experiment with two pulses, a first pulse that prepares the desired superposition state and a second pulse that drives the harmonic generation. The time delay between the two pulses adjusts the relative phase. To the best of our knowledge, such a strategy has not yet been utilized for maximizing the yield at the cutoff in high harmonic generation.

V. SUMMARY AND CONCLUSIONS

We have constructed a multi-domain pseudospectral representation of the Hamiltonian and have employed it to solve the time-dependent Schrödinger equation for the process of high order harmonic generation. The advantage of our approach is that it allows for large grids by adapting the size of each domain to the local kinetic energy. Continuity between domains is ensured by employing Gauss-Lobatto collocation and a weak formulation of the Schrödinger equation. The resulting Hamiltonian matrix is sparse, yet the representation is accurate due to accuracy of Gauss interpolation. When combined with the Chebychev propagator for time evolution, it is important to keep the spectral radius as small as possible. For a given desired accuracy, this can be achieved by a judicious choice of the number of domains and collocation order. For the example of high harmonic generation for an electron subject to a soft Coulomb potential, we have found our approach to be faster than the mapped Fourier grid method by a factor of about three.

The advantage of our approach is its stability and accuracy, besides efficiency. These features derive from the pseudospectral treatment of both spatial degree of freedom and time dependence [3, 7]. Our approach is thus particularly suitable for problems where a large grid and long propagation times are needed, for example to calculate spectra in photoionization. It can also be employed in multi-dimensional problems where the sparsity of the Hamiltonian representation will be even more important.

Efficient and accurate propagation methods are also a prerequisite in optimal control studies [2] where iterative algorithms require many propagations to maximize the figure of merit. We have benefited from the efficiency of the multi-domain pseudospectral representation of the Hamiltonian combined with Chebychev propagation to maximize the yield of high order harmonics. In particular, we have found that an initial superposition state may significantly enhance the integrated high harmonic power density. This is complementary to recent demonstrations of coherent control of high harmonic generation that have exploited high lying electronically excited states [62] and nuclear motion [63]. In our control scheme, superimposing the lowest two eigenstates with equal weights improves the harmonic yield at the so-called cutoff frequency by one order of magnitude. The relative phase in the initial superposition is found to be important, pointing to a coherent control mechanism for the harmonic yield. Such a control could be realized by a pre-pulse to prepare the initial superposition state and proper choice of the time delay of the pulse driving the harmonic generation.

ACKNOWLEDGMENTS

Financial support by the State Hessen Initiative for the Development of Scientific and Economic Excellence (LOEWE) within the focus project Electron Dynamic of Chiral Systems (ELCH) is gratefully acknowledged. This research was supported in part by the National Science Foundation under Grant No. NSF PHY11-25915. A.S. gladly acknowledges support by the Agence nationale de la recherche (contract No. ANR-12-BS04-0020).

Appendix A: Collocation with Legendre polynomials

The Legendre polynomials [4, 64] are the solutions of the second order differential equation

$$\left((1 - \xi^2) L_n'(\xi) \right)' + n(n+1) L_n(\xi) = 0, \quad (\text{A1})$$

where ' denotes the first derivative with respect to the argument of $L_n(\cdot)$. In the interval $\Lambda = [-1, 1]$, the Legendre polynomials are orthogonal with respect to the L_2 inner product and they obey the three-term recurrence relation

$$(n+1)L_{n+1}(\xi) = (2n+1)\xi L_n(\xi) - nL_{n-1}(\xi), \quad n \geq 1, \quad (\text{A2})$$

with $L_0 = 1$, $L_1 = \xi$, where $\xi \in \Lambda$. Another useful recurrence relation reads [64]

$$(2n+1)L_n(\xi) = L_n'(\xi) - L_{n-1}'(\xi), \quad n \geq 1. \quad (\text{A3})$$

In the interval $\Lambda = [-1, 1]$, the set $\{\xi_j, \omega_j^\Lambda\}$ is defined as the set of Gauss-Lobatto-Legendre nodes ξ_j and Gaussian quadrature weights w_j^Λ . It is given by [4]

$$\begin{cases} \{\xi_j\}_{0 \leq j \leq N} = \text{zeros of } \zeta(\xi) = (1 - \xi^2) L_N'(\xi) \\ \omega_j^\Lambda = \frac{2}{N(N-1)(L_N(\xi_j))^2}. \end{cases} \quad (\text{A4})$$

For moderate order collocation, the $N-1$ interior points of the Gauss-Lobatto-Legendre grid in $\Lambda = [-1, 1]$ can be generated with the help of the Golub-Welsh algorithm [65, 66]. In detail, using Eqs. (A2)-(A4) it is straightforward to find the recursion relation for $L_n(\xi)$,

$$\beta_n L_{n+1}'(\xi) + \alpha_n L_{n-1}'(\xi) - \xi L_n'(\xi) = 0, \quad (\text{A5a})$$

where the recursion coefficients α_n and β_n are given by

$$\alpha_n = \frac{n+1}{2n+1} \quad \text{and} \quad \beta_n = \frac{n}{2n+1} \quad (\text{A5b})$$

Taking into account Eq. (A4), i.e., $L_N'(\xi_j) = 0$ for all $j = 1, \dots, N-1$, the tridiagonal Jacobian matrix reads

$$\begin{pmatrix} 0 & \beta_1 & 0 & 0 & \dots & 0 \\ \alpha_2 & 0 & \beta_2 & 0 & \dots & 0 \\ \vdots & \ddots & 0 & \ddots & & 0 \\ 0 & \dots & \alpha_n & 0 & \beta_n & 0 \\ \vdots & 0 & \dots & \ddots & \ddots & 0 \\ 0 & \dots & \dots & 0 & \alpha_{N-1} & 0 \end{pmatrix} \begin{pmatrix} L'_1(\xi_j) \\ L'_2(\xi_j) \\ \vdots \\ L'_n(\xi_j) \\ \vdots \\ L'_{N-1}(\xi_j) \end{pmatrix} = \xi_j \begin{pmatrix} L'_1(\xi_j) \\ L'_2(\xi_j) \\ \vdots \\ L'_n(\xi_j) \\ \vdots \\ L'_{N-1}(\xi_j) \end{pmatrix}, \quad (\text{A5c})$$

where the eigenvalues correspond to the $N - 1$ roots of $L'_N(\xi_j)$ which define, according to Eq. (A4), the interior points of the Gauss-Lobatto grid. The extrema are given by $\xi_0 = -1$ and $\xi_N = 1$. Alternatively, in particular for a high-order quadrature, it is suitable to use a Newton-root-finding iterative method in order to avoid round-off errors that may occur during the diagonalization of the Jacobian matrix.

A first order Taylor expansion of $\zeta(\xi)$, defined in Eq. (A4), around the j th Gauss-Lobatto-Legendre point, i.e., the j th root of $\zeta(\xi)$, gives

$$\begin{aligned} \zeta(\xi) &\simeq \zeta(\xi_j) + \zeta'(\xi_j)(\xi - \xi_j) + \mathcal{O}(|\xi - \xi_j|)^2 \\ &= \zeta'(\xi_j)(\xi - \xi_j), \end{aligned} \quad (\text{A6})$$

since, by definition, $\zeta(\xi)$ vanishes at the Gauss-Lobatto-Legendre points, $\zeta(\xi_j) = 0$. Equations (A4) and (A6)

yield an explicit expression of the Legendre cardinal function $\delta^\Lambda(\xi - \xi_j)$,

$$\delta^{(\Lambda)}(\xi - \xi_j) = \frac{\zeta(\xi)}{\zeta'(\xi_j)(\xi - \xi_j)} = \frac{L'_N(\xi)(1 - \xi^2)}{(L'_j(\xi)(1 - \xi^2))'} \frac{1}{(\xi - \xi_j)},$$

where $\zeta(\xi)$ is defined in Eq. (A4) and L_j denotes the j th Legendre polynomial. Together with Eq. (A1), this yields

$$\delta^{(\Lambda)}(\xi - \xi_j) \equiv -\frac{L'_N(\xi)(1 - \xi^2)}{N(N + 1)L_N(\xi_j)} \frac{1}{\xi - \xi_j} \quad (\text{A7})$$

Moreover, we have $\delta^{(\Lambda)}(\xi_i - \xi_j) = \delta_{ij}$ at each ξ_j by construction which results in the first order differentiation matrix for Legendre cardinal functions, cf. Eq. (18).

-
- [1] D. J. Tannor, *Introduction to Quantum Mechanics: A Time-Dependent Perspective* (Univ. Science Books, Sausalito, Calif., 2007).
- [2] S. J. Glaser, U. Boscain, T. Calarco, C. P. Koch, W. Köckenberger, R. Kosloff, I. Kuprov, B. Luy, S. Schirmer, T. Schulte-Herbrüggen, D. Sugny, and F. K. Wilhelm, *Eur. Phys. J. D* **69**, 279 (2015).
- [3] R. Kosloff, *J. Phys. Chem.* **92**, 2087 (1988).
- [4] J. P. Boyd, *Chebyshev and Fourier Spectral Methods*, 2nd ed. (Dover Publications, Inc., New York, 2000).
- [5] J. C. Light and T. Carrington, *Adv. Chem. Phys.* **114**, 263 (2007).
- [6] R. Kosloff, in *Dynamics of Molecules and Chemical Reactions*, edited by R. Wyatt and J. Zhang (Marcel Dekker, New York, 1996) pp. 185–230.
- [7] R. Kosloff, *Annu. Rev. Phys. Chem.* **45**, 145 (1994).
- [8] H. Tal-Ezer and R. Kosloff, *J. Chem. Phys.* **81**, 3967 (1984).
- [9] U. Peskin and N. Moiseyev, *J. Chem. Phys.* **99**, 4590 (1993).
- [10] M. Ndong, H. Tal-Ezer, R. Kosloff, and C. P. Koch, *J. Chem. Phys.* **132**, 064105 (2010).
- [11] H. Tal-Ezer, R. Kosloff, and I. Schaefer, *J. Sci. Comput.* **53**, 211 (2012).
- [12] E. Fattal, R. Baer, and R. Kosloff, *Phys. Rev. E* **53**, 1217 (1996).
- [13] V. Kokouline, O. Dulieu, R. Kosloff, and F. Masnou-Seeuws, *J. Chem. Phys.* **110**, 9865 (1999).
- [14] K. Willner, O. Dulieu, and F. Masnou-Seeuws, *J. Chem. Phys.* **120**, 548 (2004).
- [15] S. Kallush and R. Kosloff, *Chem. Phys. Lett.* **433**, 221 (2006).
- [16] M. Nurhuda and F. H. M. Faisal, *Phys. Rev. A* **60**, 3125 (1999).
- [17] R. Heather and H. Metiu, *J. Chem. Phys.* **86**, 5009 (1987).
- [18] A. Keller, *Phys. Rev. A* **52**, 1450 (1995).
- [19] A. Karamatskou, S. Pabst, Y.-J. Chen, and R. Santra, *Phys. Rev. A* **89**, 033415 (2014).
- [20] J. L. Krause, K. J. Schafer, and K. C. Kulander, *Phys. Rev. A* **45**, 4998 (1992).
- [21] S. Chelkowski, T. Zuo, O. Atabek, and A. D. Bandrauk, *Phys. Rev. A* **52**, 2977 (1995).
- [22] K. C. Kulander and B. W. Shore, *J. Opt. Soc. Am. B* **7**, 502 (1990).
- [23] R. Santra and L. S. Cederbaum, *Phys. Rep.* **368**, 1 (2002).
- [24] J. Muga, J. Palao, B. Navarro, and I. Egusquiza, *Phys. Rep.* **395**, 357 (2004).
- [25] L. Greenman, P. J. Ho, S. Pabst, E. Kamarchik, D. A. Mazziotti, and R. Santra, *Phys. Rev. A* **82**, 023406 (2010).
- [26] N. Rohringer and R. Santra, *Phys. Rev. A* **79**, 053402 (2009).
- [27] P. Wopperer, *Electron photoemission from sodium and carbon clusters*, Theses, Université Paul Sabatier -

- Toulouse III ; Universität Erlangen-Nürnberg (2013).
- [28] L. Greenman, C. P. Koch, and K. B. Whaley, *Phys. Rev. A* **92**, 013407 (2015).
- [29] Y. Ohtsuki, W. Zhu, and H. Rabitz, *J. Chem. Phys.* **110**, 9825 (1999).
- [30] R. E. Goetz, A. Karamatskou, R. Santra, and C. P. Koch, *Phys. Rev. A* **93**, 013413 (2016).
- [31] S. Pabst, L. Greenman, P. J. Ho, D. A. Mazziotti, and R. Santra, *Phys. Rev. Lett.* **106**, 053003 (2011).
- [32] E. Tiesinga, C. J. Williams, and P. S. Julienne, *Phys. Rev. A* **57**, 4257 (1998).
- [33] R. González-Férez and C. P. Koch, *Phys. Rev. A* **86**, 063420 (2012).
- [34] A. Crubellier, R. González-Férez, C. P. Koch, and E. Luc-Koenig, *New J. Phys.* **17**, 045020 (2015).
- [35] “Weak formulation of elliptic problems,” in *Elliptic Equations: An Introductory Course* (Birkhäuser Basel, Basel, 2009) pp. 35–42.
- [36] R. B. Lehoucq, D. C. Sorensen, and C. Yang, “Arpack users guide: Solution of large scale eigenvalue problems by implicitly restarted arnoldi methods.” (1997).
- [37] C. Leforestier, R. Bisseling, C. Cerjan, M. Feit, R. Friesner, A. Guldberg, A. Hammerich, G. Jolicard, W. Karlein, H.-D. Meyer, N. Lipkin, O. Roncero, and R. Kosloff, *J. Comput. Phys.* **94**, 59 (1991).
- [38] A. Quarteroni and A. Valli, *Domain decomposition methods for partial differential equations*, reprinted ed., Numerical mathematics and scientific computation (Clarendon Press, Oxford [u.a.], 2005).
- [39] A. Toselli and O. B. Widlund, *Domain decomposition methods : algorithms and theory*, Springer series in computational mathematics, Vol. 34 (Springer, Berlin [u.a.], 2005).
- [40] P. Nevai, *Trans. Amer. Math. Soc.* **282**, 669 (1984).
- [41] V. Szalay, *J. Chem. Phys.* **99**, 1978 (1993).
- [42] C. P. Koch and R. Moszyński, *Phys. Rev. A* **78**, 043417 (2008).
- [43] B. Guo and I. Babuška, *Comput. Mech.* **1**, 203 (1986).
- [44] I. Babuška and B. Szabo, *Int. J. Num. Meth. Eng.* **18**, 323 (1982).
- [45] E. Rank, M. Rücker, A. Düster, and H. Bröker, *Int. J. Num. Meth. Eng.* **52**, 589 (2001).
- [46] C. Joachain, N. Kylstra, and R. Potvliege, *Atoms in Intense Laser Fields* (Cambridge University Press, 2012).
- [47] A. de Bohan, P. Antoine, D. B. Milošević, and B. Piraux, *Phys. Rev. Lett.* **81**, 1837 (1998).
- [48] H. Niikura, D. M. Villeneuve, and P. B. Corkum, *Phys. Rev. Lett.* **94**, 083003 (2005).
- [49] J. C. Baggese and L. B. Madsen, *J. Phys. B* **44**, 115601 (2011).
- [50] A. D. Bandrauk, S. Chelkowski, D. J. Diestler, J. Manz, and K.-J. Yuan, *Phys. Rev. A* **79**, 023403 (2009).
- [51] L. Keldysh, *Sov. Phys. JETP* **20**, 1307 (1965).
- [52] M. Lewenstein and A. L’Huillier, “Principles of single atom physics: High-order harmonic generation, above-threshold ionization and non-sequential ionization,” in *Strong Field Laser Physics*, edited by T. Brabec (Springer New York, New York, NY, 2009) pp. 147–183.
- [53] P. B. Corkum, *Phys. Rev. Lett.* **71**, 1994 (1993).
- [54] M. Lewenstein, P. Balcou, M. Y. Ivanov, A. L’Huillier, and P. B. Corkum, *Phys. Rev. A* **49**, 2117 (1994).
- [55] J. Werschnik and E. K. U. Gross, *J. Phys. B* **40**, R175 (2007).
- [56] I. Schaefer and R. Kosloff, *Phys. Rev. A* **86**, 063417 (2012).
- [57] J. Solanpää, J. A. Budagosky, N. I. Shvetsov-Shilovski, A. Castro, A. Rubio, and E. Räsänen, *Phys. Rev. A* **90**, 053402 (2014).
- [58] Y. Chou, P.-C. Li, T.-S. Ho, and S.-I. Chu, *Phys. Rev. A* **91**, 063408 (2015).
- [59] A. Castro, A. Rubio, and E. K. U. Gross, *Eur. Phys. J. D* **88**, 191 (2015).
- [60] A. Gordon, R. Santra, and F. X. Kärtner, *Phys. Rev. A* **72**, 063411 (2005).
- [61] R. E. Goetz, M. Merkel, A. Karamatskou, R. Santra, and C. P. Koch, *Phys. Rev. A* **94**, 023420 (2016).
- [62] S. Beaulieu, S. Camp, D. Descamps, A. Comby, V. Wanie, S. Petit, F. Légaré, K. J. Schafer, M. B. Gaarde, F. Catoire, and Y. Mairesse, *Phys. Rev. Lett.* **117**, 203001 (2016).
- [63] M. Lara-Astiaso, R. E. F. Silva, A. Gubaydullin, P. Rivière, C. Meier, and F. Martín, *Phys. Rev. Lett.* **117**, 093003 (2016).
- [64] J. Milton and I. A. Stegun, *Handbook of Mathematical Functions* (Dover Publications, Inc., New York, 1965).
- [65] G. Golub and G. Meurant, *Matrices, Moments and Quadrature with Applications*, Princeton Series in Applied Mathematics (Princeton University Press, 2009).
- [66] G. H. Golub and J. H. Welsch, *Mathematics of Computation* **23**, 221 (1969).